euronoise

Hybrid photoacoustic - ultrasound transmission parameter imaging in a miniature photoacoustic imager

Srirang Manohar[a], Rene Willemink[b], Johan Van Hespen[a] and Ton Van Leeuwen[c]

[a]University of Twente, Biophysical Engineering Group (BPE), Faculty of Science and Engineering (TNW), P.O. Box 217, 7500 AE Enschede, Netherlands
[b]University of Twente, Signals and Systems Group (SaS), Faculty of Electrical Engineering, Mathematics and Computer Sciences (EWI), P.O. Box 217, 7500AE Enschede, Netherlands
[c]Univ. of Twente, P.O. Box 217, 7500 AE Enschede, Netherlands
s.manohar@tnw.utwente.nl

We build on our earlier concept of extracting speed-of-sound maps of objects under photoacoustic investigation, by imaging acoustic attenuation as well. The method uses a strong absorber of light which is placed in the path of the light illuminating the sample. This acts as a source of ultrasound whose interaction with the sample can be measured at the far-end of the sample using the same ultrasound detector used for photoacoustics. Such measurements are made at various angles around the sample in a computerized tomography approach. The ultrasound transients at the multi-element detector at all projections are analyzed for both times-of-arrival and amplitude. Using a fan-beam projection reconstruction algorithm we obtain hybrid images of optical absorption, speed-of-sound and acoustic attenuation. We validate the method on an appropriate phantom.

1 Introduction

Near-infrared photoacoustic imaging is enjoying much attention in the recent past [1] in the imaging of various pathological states related to vascular condition and function. Some important applications include breast cancer detection [2, 3], skin cancer visualization [4] and burn wound depth estimation [5, 6].

The technique combines the advantages of optical imaging with those of ultrasound imaging. Optical imaging utilizes the high contrast exhibited by chromophores in the blood such as hemoglobin and oxy-hemoglobin, but suffers from poor resolution. Ultrasound imaging possesses higher resolutions due to the 2-3 orders lower scattering experienced compared with light, and scalable with frequency, but is hampered by poor vascular contrast.

Using illumination with a narrow pulse width, causes ultrasound to be generated at absorbing sites in tissue, by the process of thermoelastic expansion. Non-radiative deexcitation of the absorbed light results in heat energy being emitted, the resulting temperature rise drives a thermal expansion that results in a pressure build up. This then relaxes by the propagation of ultrasound waves which can be detected at the surface of the medium using conventional ultrasound detectors. The signals can be processed in a similar manner as in ultrasound imaging leading to mapping of the optical absorption in the medium.

One of the inputs for reconstruction algorithms, which are usually based on one or other form of backprojection algorithms [7] is the speed-of-sound of the medium through which the ultrasound propagates. This is used to translate the time-of-arrival of the ultrasound pulses into distance information in image space. In most cases the speed-of-sound for tissue is not known precisely, and the assumption of an incorrect speed-of-sound (SOS) for reconstruction could lead to improper backprojections leading to compromised resolution and contrast.

Recently, we presented a novel methodology [8 - 10] which could be easily applied to existing computed tomography (CT) type photoacoustic imagers, where the addition of a strong absorber with low cross-sectional area allows the measurement of SOS. The strong absorber acts as a source of ultrasound which interacts with the object under investigation and the resulting ultrasound waves are detected at the far end of the object using a linear ultrasound array. Measurement of the time-of-arrival (TOA) and with knowledge of the geometry of would result in an estimation of the integrated SOS between the passive element and the respective element of the array. This defines a projection of the SOS of the object. Obtaining such projections around the object over 360° permits the reconstruction of the SOS of the object.

The first results of such measurements and analysis were presented recently [8, 9]. Further to the imaging of SOS maps, the signals that propagate through the object also contain information about the acoustic attenuation in the changes in amplitude of the signals. The acoustic attenuation map of the object can then be similarly reconstructed as in the case of an SOS map, except that projections in this case would then be the projections of integrated acoustic attenuation. A few results of the mapping of acoustic attenuation of a phantom are presented in this article.

2 Materials and Methods

2.1 Photoacoustic Computed Tomography scanner

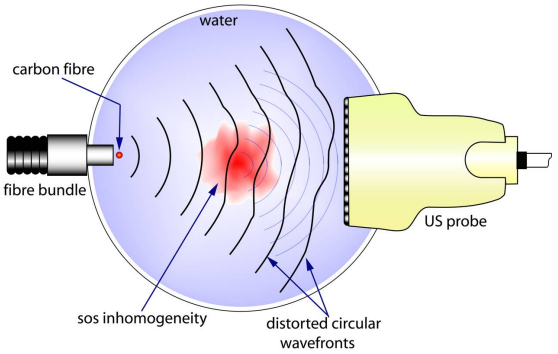

Fig.1 Schematic of the setup showing the concept of speed-of-sound/acoustic attenuation imaging using photoacoustics. The addition to the standard imager is a carbon-fiber introduced at the position of illumination.

Figure 1 shows the schematic of a typical computerized tomography (CT) photoacoustic (PA) imager, with a photograph of the instrument in Figure 2. This is a miniature scanner that is used for studying small-animals such as mice. The object under investigation is mounted on a rotary stage to be suspended in water in an imaging tank. The rotary stage is driven by a stepper motor. The stage is mounted on a platform which forms the payload to a linear stage which is arranged vertically. A 128 element ultrasound array (Esaote B.V., Maastricht, The Netherlands) is fitted on the side of the imaging tank opposite to the location of the fiber bundle. The fiber bundle transports pulsed near-infrared (NIR) light from an Nd:YAG laser 5 ns pulse widths, 10 Hz repetition rate to illuminate the object. Ultrasound is produced in the object by the PA effect, which propagates through the water to be detected by the detector elements; this is a projection. The detector is connected via a 128:4 MUX to a data acquisition

system (DC265, Acqiris cc103, Switzerland). The object is then rotated in angular steps of 3° covering 360° recording projections at each angle which may be reconstructed based on algorithms based on backprojection [7], leading to the photoacoustic image of the object.

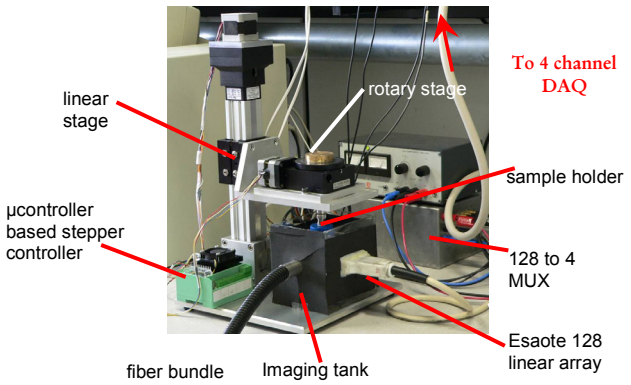

Fig.2 Photograph of prototype instrument.

For the SOS and acoustic attenuation part, a carbon fiber 250 µm is positioned in the imaging tank in front of the fiber bundle to be in the path of light illuminating the object. The carbon fiber absorbs the light incident on it setting up an ultrasound transient by the photoacoustic effect. The carbon fiber ensures that the acoustic waves which are produced fan out in the imaging plane but are restricted in the plane orthogonal to this. The otherwise circular wavefront in the plane is distorted as the wave interacts with the object. Where regions of higher acoustic velocity are encountered there is an advancement of the wavefront; retardation of the wavefront occurs when regions of lower SOS are encountered. The pulse propagates through the object to be collected at the far-end by the individual elements of the ultrasound probe. The times-of-arrival (TOA) of the pulse and the amplitudes can then be extracted at each element.

Instead of measuring the information directly, a reference measurement can be made retracting the object allowing the ultrasound to propagate in water alone. In such a case undistorted circular wavefronts can be expected which are then recorded at each element. Measurements were performed with roughly 30 mJ of energy at 1064 nm using 10 averages.

2.2 Speed-of-sound and acoustic attenuation phantoms

We investigated the acoustic transmission properties of carbon particle doped agar gel samples which has been studied earlier by Madsen and collaborators [11, 12].

Carbon particles (Sigma-Aldrich) ranging from 2-12 µm in diameter of various concentrations were added to 3 % aqueous solutions of agar. The mixture was continuously stirred to avoid the clustering of carbon particles. Some care had to be taken when higher carbon contents were used since clustering caused inhomogeneities to be formed within the sample but also made them fragile. The through-transmission properties of various such samples mounted on a reflector in an imaging tank were measured using a pulser-receiver (Panametrics, Square wave Pulser Receiver) driving a 5 MHz transducer (Panametrics-NDT,V310, 0.25". The pulsed signals were recorded using a data acquisition system (DC265, Acqiris, Switzerland). The signals were analyzed using standard methods for extracting speeds-of-sound and acoustic attenuation.

The results for various samples as a function of concentration of carbon particles are consolidated in Fig. 3. It is seen that linear variations in both properties are available.

We decided to use for the first feasibility studies a simple phantom which is shown in Fig. 4. The phantom consisted of a 3% agar gel cylinder of 80 mm length and 26 mm diameter. This possessed 2 cavities: one with a square cross-section of 5 mm side and the other circular cross-section of 6 mm diameter. These were filled with the carbon doped aqueous solutions of 3 % agar, with a 1 % and 2 % concentrations of carbon for the square and circular cavities respectively. These concentrations were chosen rather arbitrarily to provide a sufficient contrast for imaging. From the characterization studies the properties of the inhomogeneities was well known. (The square inhomogeneity had α_s=0.65 dB cm^{-1}, v_s=1499 ms^{-1}; the circular inhomogeneity had α_s=1 dB cm^{-1}, v_s=1501 ms^{-1};)) The cylindrical phantom was terminated in a coupler that allowed easy mounting onto the rotary stage of the imager.

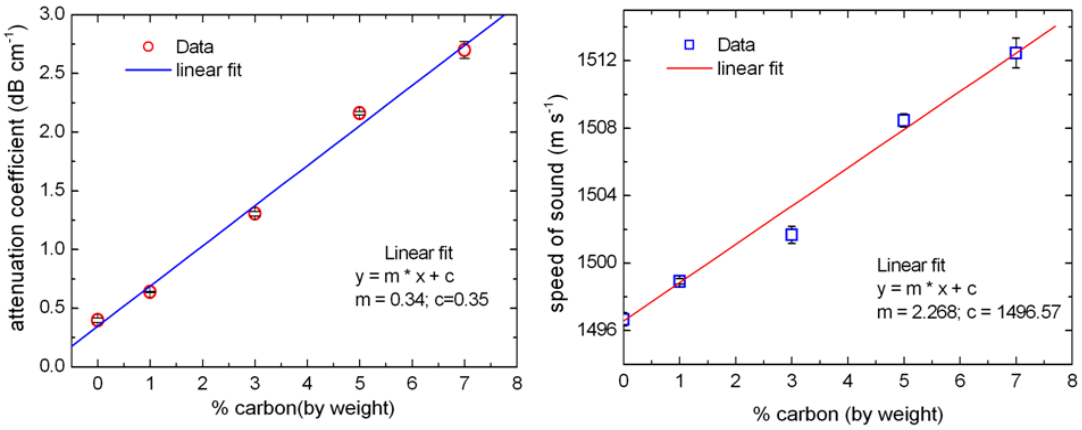

Fig.3 (left) Attenuation coefficient as a function of carbon concentration in 3 % agar gel. (right) Speed-of-sound as a function of carbon concentration in 3 % agar gel.

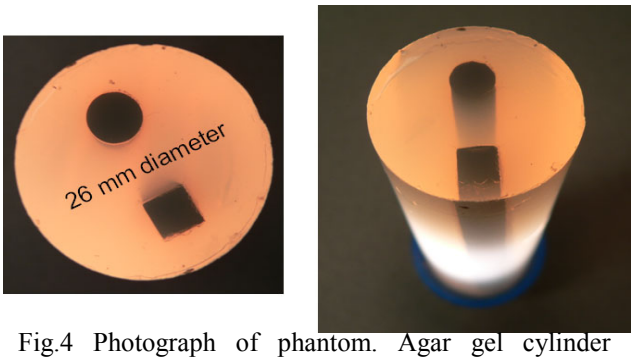

Fig.4 Photograph of phantom. Agar gel cylinder mounted on a coupler to the rotary stage. The phantom has two inhomogeneities with SOS and acoustic attenuation contrasts compared with background.

2.3 Estimation of integrated speed-of-sound

The speed-of-sound may be calculated in the time domain or the frequency domain. In a first approximation, the time-of-arrival (TOA) of the ultrasound transient at a detector element is the line integral of the inverse of the SOS distribution encountered by a ray traversing the path from source to the detector. The normalized TOA at element n is:

$$\Delta t_n = \int_{l(\phi,n)} \frac{ds}{v_s} - \int_{l(\phi,n)} \frac{ds}{v_w}$$

where l is the ray-path defined by rotation angle Φ and detector position n, $v_w(v_s)$ are the acoustic velocities in water (sample). The normalized TOA is obtained by a cross-correlation between the signals at every element position when the object is present, with their corresponding signals when the object has been retracted. In such a case the time-of-arrival (TOA) difference between sample and water, at an element position for a certain angle is obtained.

The group velocity may then be calculated as:

$$v_s = \frac{v_w}{1 + \frac{v_w \Delta t_n}{l(\phi,n)}}$$

However, in tissue due to frequency dependent attenuation, dispersion will be present, which causes various phase components of the broadband pulse to travel at different velocities. This could lead in cases to distortion in the signal shapes making a time-domain analysis by cross-correlation inaccurate.

In such cases, the phase spectral method may be used which is performed in the frequency domain. Here the FFTs of the sample and water signal are obtained; the phases are subtracted from each other to yield the phase difference of the frequency component in the sample and that in water. From this the phase velocities may be calculated as:

$$v_s(\omega) = \frac{v_w}{1 + \frac{v_w \Delta\phi(\omega)}{l(\phi,n)}}$$

For the phantoms that we use, the differences between the cross-correlation method and the phase-spectral method at the central frequency of the transducer are negligible since the phantoms are not expected to have any considerable dispersion. However, the phase-spectral method is more appropriate for tissue and it is advisable to use the frequency domain method for estimating SOS.

2.4 Estimation of integrated acoustic attenuation

In a similar way to SOS, the acoustic attenuation may be calculated in the time domain or in the frequency domain. In the first approximation, neglecting interface losses and under the assumption of negligible water attenuation, a ratio of amplitudes with and without the object in water, leads to the acoustic attenuation:

$$\alpha_s(\mathrm{dB}) = 20\log_{10}\left\{\frac{A_s(t)}{A_w(t)}\right\}$$

In the log-spectral method, the amplitudes of the spectral components are treated as:

$$\alpha_s(\omega) = 20\log_{10}\left\{\left|\frac{A_s(\omega)}{A_w(\omega)}\right|\right\} \mathrm{dB}$$

In a more realistic scenario the attenuation is frequency dependent. Attenuation of most materials follows a frequency power law [13]:

$$\alpha_s(\omega) = \alpha_0 \left|\omega^y\right|$$

where α_0 is the material dependent attenuation constant and y is a material dependent parameter that ranges between 0 and 2. Specifically, in a realistic scenario in soft tissue, the parameter $y = 1$. In this case, estimation of the attenuation constant can be done in the frequency domain by fitting the data to the expected frequency dependent attenuation function. In such a case errors due to interface losses are minimized since these are expected to be constant and not dependent on frequency.

2.5 Reconstruction of Acoustic Property Distributions

Once projections of both the integrated parameters for estimating SOS and acoustic attenuation have been obtained, the acoustic property maps have to be reconstructed. The unknown acoustic property distribution is discretized by sampling over a grid with uniform spacing.. Each sample point on the grid represents the value of the acoustic property distribution at that location, off-grid points are interpolated via bilinear interpolation. The projection measurements can be expressed as a linear combination of a number of sample points. To construct this linear combination, a line is traced through the grid connecting the source and detector. At regular intervals a sample is taken. Bilinear interpolation is then used to express the sample as a linear combination of samples. For each projection angle and each detector element such a projection measurement is available, resulting in a linear system:

$$Hx = z,$$

where the matrix H is formed by tracing along the projection lines and the vector z represents all individual projection measurements. Since the construction of the

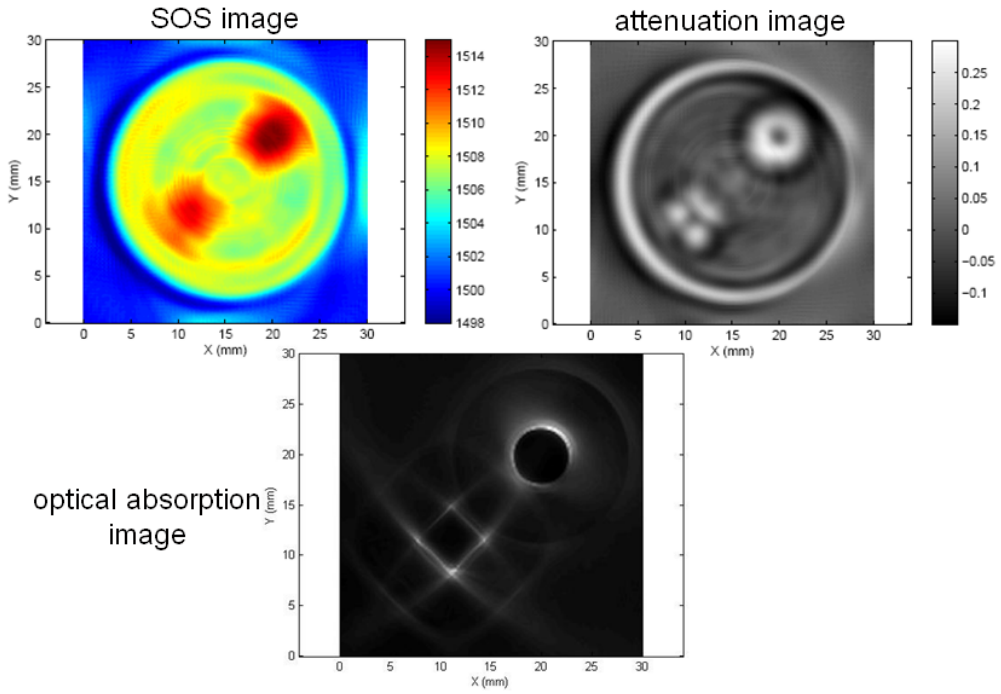

Fig.5 Results of the reconstruction of acoustic property distributions and conventional photoacoustic mapping of the phantom.

matrix *H* is based on tracing the projection lines we have to know the geometry of the complete experimental setup, i.e. the positions of the source, the detectors and the center of rotation. All of these geometrical parameters are known roughly in advance, but are fine-tuned using the water measurement as a calibration [14]. Once the projection matrix *H* is constructed, the reconstruction of the acoustic property distribution is done by solving for *x*. Since the matrix *H* is large and sparse, the linear system can efficiently be solved with the LSQR algorithm. Both the attenuation and speed of sound distribution can be reconstructed using the above outlined algorithm.

In case of the attenuation distribution, we use the integrated attenuation measurements as input and directly obtain a distribution of the attenuation constant. In case of the speed of sound distribution, the delay time between reference and object measurements is used as input resulting in an output image of the relative delay time per unit distance.

3 Results and discussions

In the experiments conducted, it was observed during the calibration measurements in water that there were discrepancies measured in both arrival times and amplitudes of the signals. Significant was the discovery that the errors were not random, but systematic with a clustering of the values of errors on the basis of detector elements chosen; residual values of the fit (both time-of-arrival and amplitudes) during the calibration were similar for groups of 4 elements [14]. The reason for the clustering is because the system multiplexes the detector elements to 4 at a time, these element outputs are affected similarly compared with others. Why the error is present in the first place is not completely known at the moment, but could be to laser output variations or due to amplifier electronics drift/instability.

The measurements are thus corrupted with an additive noise term working on all 4 sensors simultaneously. The fact that the noise on the measurements is correlated can be exploited in a noise filtering algorithm which was applied to the raw data. Details of this procedure have been recently detailed by Willemink *et al* [14], we do not go into details here.

The images of speed-of-sound, acoustic attenuation and optical absorption from the filtered data are shown in Fig. 5. The gross features of the phantom can be recognized in the 3 images. However, the values of the SOS and acoustic attenuation have not been faithfully reconstructed compared with the actual values designed into the phantoms. The photoacoustic image is seen to depict only the surfaces of the inhomogeneities.
The reason for the compromised resolution and mismatch between the estimated values and known values is attributed to the noise but also the extensive processing that the raw data have undergone to minimize the noise. The photoacoustic data shows only the outer surface of the inhomogeneities since these are highly absorbing due to their high carbon contents preventing further light penetration into the structures.

4 Conclusions

The methodology and the analysis are successful in imaging three parameters of the phantom. Such an approach permits not only functional information from conventional photoacoustics to be extracted but also anatomic and morphological information from ultrasound parameter depiction. There are however, some discrepancies in the measurements that resulted in a compromised resolution and reproduction of the exact physical values of the phantom. The electronics and laser stability are being

investigated at the moment and some solutions have been identified. Future work will concentrate on obtaining better measurements without the noise which has plagued the present experimental data. Further, when the technical difficulties have been resolved, we will make images of more complicated phantoms and finally of small animals such as mice.

Acknowledgments

This research is funded by the Institute of Biomedical Technology (BMTI) of the University of Twente via the NIMTIK program; and by SenterNovem through the project IPD067771 in the theme IOP Photonic Devices.

S.M. thanks the Netherlands Organization of Scientific Research NWO and the Technology Foundation STW for a personal grant in the Vernieuwingsimpuls program.

The authors are grateful to Yashasvi Purwar, IIT Madras, India, for performing the experiments.

References

[1] M. Xu, L. V. Wang, "Photoacoustic imaging in biomedicine", *Rev. Sci. Instrum.* 77, 04110 (2006)

[2] S. Manohar, S. R., Vaartjes, J. C. G. van Hespen, F. van den Engh, J. M. Klaase., W. Steenbergen, , T. G. Van Leeuwen, "Initial results of near-infrared imaging of the symptomatic breast using Photoacoustics," *Opt. Exp.* 15, 12277 (2007)

[3] S. Ermilov, A. Stein, A. Conjusteau, R. Gharieb, R. Lacewell, T. Miller, S. Thompson, P. Otto, B. McCorvey, T. Khamapirad, M. Leonard, A. A. Oraevsky, "Detection and noninvasive diagnostics of breast cancer with 2-color laser optoacoustic imaging system," *Proc. SPIE* 6437, pp. 643703 (2007)

[4] J. T. Oh, M. L. Li, H. F. Zhang, K. Maslov, G. Stoica, L. V. Wang, "Three-dimensional imaging of skin melanoma in vivo by dual-wavelength photoacoustic microscopy," *J. Biomed. Opt.* 11, 34032 (2006)

[5] H. F. Zhang, K. Maslov, G. Stoica, L. V. Wang., "Imaging acute thermal burns by photoacoustic microscopy," *J. Biomed. Opt.* 11, 054033 (2006)

[6] R. J. Talbert, S. H. Holan, J. A. Viator " Photoacoustic discrimination of viable and thermally coagulated blood using a two-wavelength method for burn injury monitoring," *Phys. Med. Biol.* 52, 1815 (2007)

[7] S. J. Norton, M. Linzer, "Ultrasonic reflectivity tomography: reconstruction with circular transducer arrays," *Ultrason. Imaging* 1, 154 (1979)

[8] S. Manohar, G. H. Willemink, F. van der Heijden, C. H. Slump, T. G. Van Leeuwen, "Concomitant speed-of-sound imaging in a photoacoustic imager," *Appl. Phys. Lett.* 91, 131911 (2007)

[9] G. H. Willemink, S. Manohar, F. Van der Heijden, C. H. Slump, T. G. Van Leeuwen, "Acoustic property measurements in a photoacoustic imager," *Proc. SPIE* 6631, pp. 663109 (2007)

[10] S. Manohar, G. H. Willemink, T. G. Van Leeuwen, "Speed-of-sound imaging in a photoacoustic imager," *Proc. SPIE* 6437, 64370R (2007)

[11] M. M. Burlew, E. L. Madsen, J. A. Zagzebski, R. A. Banjavic, S. W. Sum, "A new ultrasound tissue-equivalent material," *Radiology* 134, 517 (1980)

[12] K. A. Wear, T. A. Stiles, G. R. Frank, E. L. Madsen, F. Cheng, E. J. Feleppa, C. S. Hall, B. S. Kim, P. Lee, W. D. O'Brien Jr, M. L. Oelze, B. I. Raju, K. K. Shung, T. A. Wilson, J. R. Yuan, " Interlaboratory Comparison of Ultrasonic Backscatter Coefficient Measurements From 2 to 9 MHz," *J Ultrasound Med* 24, 1235 (2005)

[13] K. R. Waters, J. Mobley, G. J. Miller, "Causality-imposed (Kramers-Kronig) relationships between attenuation and dispersion," *IEEE Trans. Ultrason, Ferro Freq Control,* 52, 822 (2005)

[14] G. H. Willemink, S. Manohar, Y. Purwar, F. Van der Heijden, C. H. Slump, T. G. Van Leeuwen, "Imaging of acoustic attenuation and speed of sound maps using photoacoustic measurements," *Proc. SPIE* 6920, pp. 692013 (2008)